Quantifying 3D Live-Cell Membrane Dynamics Using Dynamic Metal-Induced Energy Transfer Spectroscopy (dynaMIET)

José Ignacio Gallea[1†], Narain Karedla[2,3†], Dongxia Wang[1,4], Bin Zhao[1], Lizhen Chen[1], Jörg Enderlein[1,5*], Tao Chen[1*]

[1]Third Institute of Physics – Biophysics, Georg August University, Friedrich-Hund-Platz 1, Göttingen, 37077, Germany.

[2]The Rosalind Franklin Institute, Harwell Campus, Didcot, OX11 OFA, UK.

[3]Botnar Institute for Musculoskeletal Sciences, Windmill Road, Oxford, OX3 7LD, UK.

[4]Department of Molecular Biology, Princeton University, Princeton, 08540, USA.

[5]Cluster of Excellence "Multiscale Bioimaging: from Molecular Machines to Networks of Excitable Cells" (MBExC), Universitätsmedizin Göttingen, Robert-Koch-Str. 40, Göttingen, 37075, Germany.

[*]Corresponding author. Email: tao.chen@phys.uni-goettingen.de; jenderl@gwdg.de

[†]These authors contributed equally to this work.

Short title: dynaMIET for Membrane 3D Dynamics

The dynamic behavior of cellular membranes underpins essential biological processes, including signal transduction, intracellular trafficking, and mechanotransduction. However, simultaneously quantifying lateral molecular diffusion and vertical membrane fluctuations in live cells remains challenging. Here, we present dynamic metal-induced energy transfer spectroscopy (dynaMIET), which integrates metal-induced energy transfer with fluorescence correlation spectroscopy

to resolve three-dimensional membrane dynamics with nanometer axial sensitivity and microsecond temporal resolution. dynaMIET enables concurrent measurement of lateral diffusion and vertical undulations within a single acquisition. We validate the method using simulations and model membranes and demonstrate its robustness in living cells, applying it to the plasma membrane, endoplasmic reticulum, and nuclear envelope. By capturing both molecular mobility and membrane fluctuations, dynaMIET provides a powerful, non-invasive tool for probing membrane mechanics and organization. This advance opens new avenues for studying membrane-associated phenomena in health and disease, including cancer cell mechanics, protein–membrane interactions, and organelle dynamics.

Teaser: dynaMIET enables simultaneous measurement of lateral diffusion and vertical membrane fluctuations in live cells.

Biological membranes are highly dynamic structures composed of a complex mixture of lipids and proteins (*1–3*). Far from being passive barriers, membranes actively regulate a wide range of cellular functions, including adhesion, signal transduction, molecular trafficking, and environmental sensing (*4–7*). These functions critically depend on the dynamic behavior of membrane components. Lipids and proteins constantly move, rotate, and interact within the bilayer, and the membrane itself undergoes spontaneous bending, stretching, and vertical fluctuations (*6, 8*). Abnormalities in these dynamic properties are closely associated with pathological conditions, including cancer (*9, 10*), neurodegenerative diseases (*11, 12*), and immune dysfunction (*13, 14*).

The physical properties of membranes, such as flexibility, tension, and curvature, are closely regulated and contribute to mechanotransduction, vesicle trafficking, and synaptic activity (*6, 15, 16*). For instance, the enhanced deformability of cancer cell membranes facilitates metastasis by promoting extravasation through tight endothelial barriers (*9, 17*). In immune cells, membrane mechanics affect the formation of immunological synapses and antigen presentation (*18, 19*). In neurons, changes in membrane composition and fluidity influence vesicle fusion and neurotransmitter release (*6, 20*). Moreover, many viruses, including SARS-CoV-2 and HIV, exploit host membrane dynamics during entry, replication, and egress (*21, 22*).

Membrane dynamics span a broad range of spatial and temporal scales. These include molecular rotations of lipids and proteins (*23, 24*), lipid flip-flop between bilayer leaflets (*25, 26*), and lateral diffusion within the membrane plane (*27, 28*), as well as micron-scale vertical undulations and bending (*29, 30*). These dynamic processes are often coordinated with the underlying cytoskeleton (*31*), and their dysregulation can indicate alterations in cell stiffness, metastatic potential, or responsiveness to drugs (*32, 33*).

Despite the fundamental importance of membrane dynamics, current experimental tools are limited. Techniques such as fluorescence recovery after photobleaching (*34*), fluorescence correlation spectroscopy (FCS) (*35*), and single-molecule tracking (*36*) effectively measure lateral diffusion of lipids and proteins, but cannot capture vertical fluctuations. Conversely, methods such as flicker spectroscopy (*37*), diffraction phase microscopy (*38, 39*), and reflection interference contrast microscopy (*40–42*) can quantify membrane fluctuations but lack molecular specificity and cannot simultaneously resolve molecular diffusion. Dynamic optical displacement spectroscopy (DODS), an FCS-based method, measures stochastic membrane undulations by positioning the membrane at the confocal focus inflection point, where undulation-induced fluorescence fluctuations dominate while single-molecule diffusion is suppressed through high-density fluorescent labeling (*29*). Recently, employing a similar dense-labeling approach, our group applied metal/graphene-induced energy transfer imaging/spectroscopy (MIET/GIET) (*43–46*) to quantify vertical membrane fluctuations with sub-nanometer precision (*44*). However, such high labeling densities are difficult to achieve in living cells due to phototoxicity and are incompatible with FCS measurements for diffusion.

Currently, no method exists that can simultaneously capture lateral diffusion and vertical membrane fluctuations both for model membrane and cellular membrane. In this study, we introduce dynamic metal-induced energy transfer spectroscopy (dynaMIET), an approach that simultaneously measure nanoscale molecular diffusion and vertical membrane fluctuations (i.e., three-dimensional (3D) membrane dynamics) with sub-millisecond temporal resolution. The dynaMIET set-up builds on the MIET, an axial super-resolution technique that localizes the molecule with nanometer precision using a thin metal film. By focusing at the metal interface while performing FCS, the detected signal contains contributions from both lateral diffusion of labeled lipids or proteins and vertical membrane undulations, each leaving a distinct signature in the fluorescence intensity au-

tocorrelation. The dynaMIET combines the high axial sensitivity of MIET with the fast, sensitive detection capabilities of FCS to resolve 3D membrane dynamics within a single measurement. This enables accurate quantification at low dye concentrations, compatible with live-cell fluorescent protein imaging, and allows axial membrane fluctuations to be disentangled from lateral molecular diffusion.

To validate our method, we first applied dynaMIET to model GUVs and benchmarked our results against established techniques. We then extended the method to biologically relevant systems, including the basal plasma membrane (PM), the endoplasmic reticulum (ER), and the nuclear envelope (NE) in both fixed and live cells. These structures play critical roles in processes such as mechanotransduction, protein synthesis, and gene regulation.

Result

Principle of dynaMIET for measuring the 3D dynamics of membranes

The 3D membrane dynamics comprises in-plane lateral diffusion and out-of-plane undulations (vertical fluctuations). In microscopic observations, lateral diffusion refers to the in-plane movement of membrane constituents (Fig. 1A), while vertical fluctuations capture out-of-plane undulations and curvature changes of the membrane (Fig. 1A). Our method, dynaMIET, enables simultaneous quantification of both types of dynamics by combining MIET with standard FCS measurements.

Fig. 1A illustrates the MIET experimental setup. A typical substrate consists of a glass coverslip coated with a thin gold film. MIET operates via electrodynamic coupling between the excited-state near-field of a fluorophore and surface plasmons in the gold layer. Functionally, the gold film acts as a non-radiative energy acceptor, analogous to the acceptor in Förster resonance energy transfer (FRET), resulting in highly distance-dependent quenching. This coupling modulates both the fluorescence lifetime and emission brightness of the fluorophore as a function of its axial (vertical) distance from the metal surface (see Supplementary Text).

As shown in Fig. 1B, theoretical calculations for a dye whose transition dipole rotates freely and is oriented randomly with respect to the substrate (quantum yield $\phi = 1$, emission wavelength $\lambda_{\mathrm{em}} = 690$ nm) predict that the relative fluorescence lifetime $\tau_f(h)/\tau_0$ increases monotonically

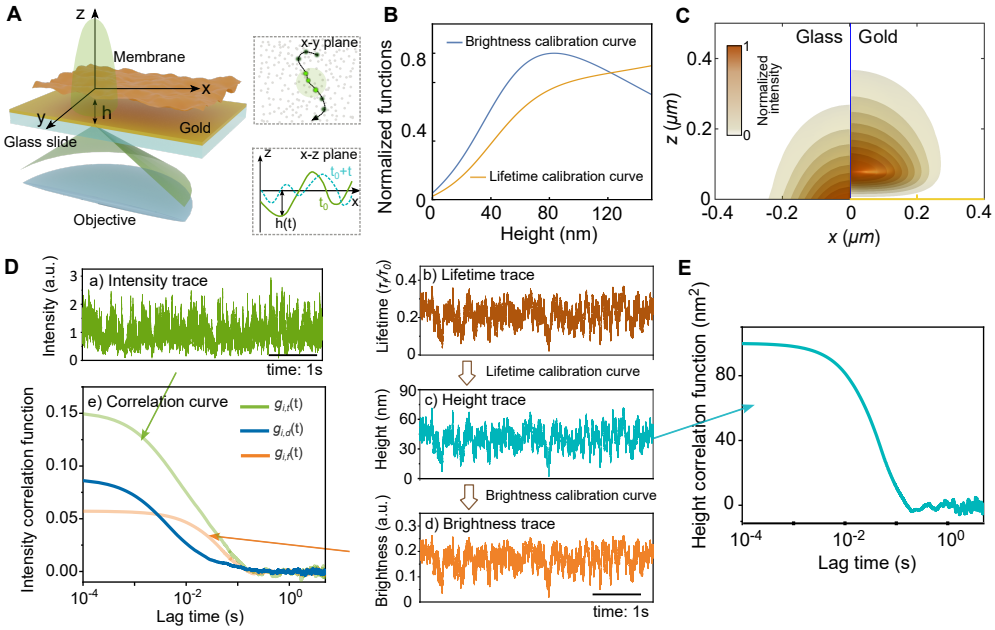

Figure 1: **Principle of dynaMIET for measuring membrane dynamics.** (A) Sketch of the membrane dynamics within a confocal volume. The coordinate system and notations are defined. The membrane is in the x-y plane and undergoes small displacements in the z direction. Lateral dynamics refer to the diffusion of fluorophores within the x–y plane, while vertical dynamics correspond to the up-and-down fluctuations of the membrane along the z axis. A fluctuating membrane situated above a gold film is schematically depicted. The double-headed arrow indicates the average height h of the labeled membrane from the substrate. (B) Calculated relative fluorescence lifetime (τ_f/τ_0) (upper panel) and relative brightness (lower panel) of an emitter as a function of its distance h from a MIET substrate. For details of calculation parameters, see Fig. S12. (C) Comparison of calculated iso-surfaces of molecular brightness as a function of position within a confocal focus (N.A. = 1.49) of a circular polarized beam, with the focal plane positioned at the glass–sample interface, for both a glass substrate and a MIET substrate. For details of calculation, see Supplementary Text 4 and Fig. S13. (D) Simulation for a fluctuating membrane above a gold surface. Simulated fluorescence intensity trace (a) and lifetime time trace (b). Calculated height trace (c) and brightness trace (d) based on the calibration curves in **b**. (e) Calculated intensity correlation curves. (E) Calculated height correlation curve from **D-c**.

with height h (at least over $h \lesssim 150$ nm), whereas the brightness $b(h)$ rises with h and reaches a maximum near $h \approx 90$ nm before decreasing at larger separations. This axial brightness dependence is steep over the first few tens of nanometers (Fig. 1 B,C). Consequently, small vertical displacements of molecules produce large fractional intensity changes. Notably, the brightness decrease beyond 90 nm in Fig. 1B is caused by the concurrent decline in collection efficiency and excitation intensity with increasing distance from the surface (see Fig. S12)

In conventional FCS (i.e., without a MIET/gold substrate) axial fluctuations contribute little because the confocal detection function varies only weakly over nanometer scales along z (its axial extent is on the order of ~ 300 nm). Consequently, small vertical displacements lead to negligible intensity modulation, and the measured fluctuations mainly report on lateral diffusion within the confocal volume.

In contrast, in the presence of a MIET substrate, the detected intensity becomes strongly sensitive to axial motion. Accordingly, the measured intensity autocorrelation function (iACF) , denoted by $g_{i,t}(t)$, reflects both lateral and vertical dynamics:

$$g_{i,t}(t) = g_{i,d}(t) \cdot g_{i,f}(t) \cdot g_{i,tri}(t) \tag{1}$$

Here, $g_{i,d}(t)$ describes lateral diffusion, $g_{i,f}(t)$ captures vertical fluctuations, and $g_{i,tri}(t)$ accounts for the triplet-state relaxation of the fluorophore. In general, triplet relaxation occurs on the microsecond timescale and does not interfere with the slower membrane dynamics that unfolds on the millisecond timescale. A key challenge here is disentangling the respective contributions of molecular diffusion and vertical membrane fluctuations to the total iACF, which take place on similar timescales. In our previous work, we addressed this by increasing the density of labeling in the bilayers, which suppresses diffusion-related fluctuations due to the larger number of emitters in the detection volume (*44*). However, this strategy inevitably comes at the cost of reducing the access to valuable diffusion information on the constituent proteins or lipids.

To overcome this, we developed a strategy that leverages concurrent determination of the fluorescence lifetime, molecular height, and brightness from the raw photon data. In a typical lifetime-based point measurement using time-correlated single-photon counting (TCSPC), two principal observables are obtained: the fluorescence lifetime trace and the fluorescence intensity trace. Because the axial position of the membrane is determined exclusively from the fluorescence

lifetime, the lifetime trace allows for analyzing height-related vertical fluctuations of the membrane ($g_{i,f}(t)$). In contrast, the fluorescence intensity trace is determined by the total temporal fluctuations arising from all dynamics processes ($g_{i,t}(t)$). Aditionally, we used eq 1 to isolate and quantify the lateral diffusion component ($g_{i,d}(t)$). To demonstrate this approach, we simulated the 3D dynamics of a lipid membrane near a MIET substrate as observed in a confocal setup (see Methods for detailed information on the simulations). Fig. 1D shows (D-a) a simulated fluorescence intensity trace used to calculate the total iACF $g_{i,t}(t)$ and (D-b) a corresponding lifetime trace for a fluctuating membrane. These simulations faithfully replicate the experimental data acquired via time-tagged time-resolved (TTTR) single-photon counting.

We then convert the simulated lifetime trace into a height trajectory $h(t)$ (Fig.1D-c) using a calibration curve derived from MIET theory (see Fig.1B). The height trace is further transformed into a corresponding relative brightness trace using the calculated brightness-vs.-height curve (see Fig.1B). This yields a synthetic trace from which we compute the fluctuation-only iACF component $g_{i,f}(t)$. Using Eq.(1), we isolate the diffusion-related autocorrelation function $g_{i,d}(t)$ by dividing the total iACF by $g_{i,f}(t) \cdot g_{i,tri}(t)$. The lateral diffusion coefficient D is then extracted using established 2D diffusion models applicable to lipid bilayers (*35*).

For a fluctuating membrane, the instantaneous vertical position is time-dependent, and the height trajectory $h(t)$ can be decomposed into a time-averaged mean height h_0 and the time-dependent instantaneous displacement $\delta h(t)$, such that $h(t) = h_0 + \delta h(t)$. The temporal behavior of vertical membrane fluctuations is characterized by the height autocorrelation function (hACF), $g_h(t) = \langle \delta h(t')\delta h(t'+t)\rangle_{t'}$ (Fig. 1E). The amplitude of $g_h(t)$ yields the amplitude of the variation of root mean square fluctuation $\psi = \sqrt{\langle \delta h^2 \rangle}$, while the characteristic decay time τ^* represents the relaxation timescale of vertical fluctuations (*29, 44*). In the analysis, the fluctuation amplitude ψ was determined from the mean-square intercept of the hACF, i.e., its value at $\tau \equiv 10^{-4}s$) and the relaxation time τ^* was defined as the time point at which $g_h(\tau^*) \equiv g_h(0)/e$. Based on these analyses and fitting, we obtained diffusion coefficient D = 4.97 ± 0.15 μm^2/s (mean ± SD, n = 10 independent simulations) and fluctuation amplitude ψ = 9.96 ± 0.03 nm (mean ± standard deviation (SD), n = 10 independent simulations) for the simulated data, which closely match the input values used in the simulation (D = 5 μm^2/s and ψ = 10 nm).

When transitioning from simulations to experimental dynaMIET, the data analysis must ex-

plicitly account for model experimental photophysics such as photobleaching, triplet-state kinetics, and detector artifacts such as afterpulsing. Additionally, in our workflow, we couple fluorescence intensity-lifetime information via rigorous fluorescence lifetime fitting. These components are integrated into our custom analysis pipeline, which is described in detail in the Materials and Methods section. In addition, MIET sensitivity is influenced by the properties of the fluorescent probes such as their emission spectrum and quantum yield, as they directly determine the lifetime-to-distance and distance-to-brightness calibration curves (*47–49*). In particular, the quantum yield affects the effective MIET working distance (*47*). Similarly, probes with longer fluorescence lifetimes are advantageous, as they improve distance sensitivity and the accuracy of lifetime–distance conversion (*50*). Concerning labeling geometry, for the dynamic measurements presented here, the fast rotational diffusion of the fluorophores justifies the assumption of a random orientation (*44*). Finally, an important prerequisite of MIET measurements is the assumption that the fluorescence lifetime is only modulated by the metal but otherwise homogeneous. We checked this by control measurements of our samples on pure glass, which verified the absence of any lifetime variation or lifetime heterogeneity.

3D dynamics of GUV membranes

We validated dynaMIET by measuring membrane undulations and lipid diffusion in the proximal membrane of deflated giant unilamellar vesicles (GUVs), and then compared our measurements with well-established theoretical predictions (*51–54*), previous experimental results (*29, 44, 51–53*), and a comparison with a planar membrane without bending undulations. GUVs were prepared from 1-stearoyl-2-oleoyl-sn-glycero-3-phosphocholine (SOPC) lipids and fluorescently labeled 1,2-Dipalmitoyl-sn-glycero-3-phosphoethanolamine (DPPE-Atto655) in a labeling ratio of 0.05 mol % by electroformation in a sucrose solution with an osmotic pressure of 230 mOsm/L. For fluorescence measurements, GUVs with an internal sucrose concentration of 230 mOsm/L were immersed in a hypertonic solution of 400 mOsm/L and added above a MIET substrate passivated with bovine serum albumin (BSA). The MIET substrate comprised a 10 nm thick silica layer and a 10 nm gold film on a glass coverslip. The elevated osmolarity outside the GUVs led to their deflation and reduction of membrane tension, inducing membrane undulations close to the substrate surface (*29, 55*). FCS

measurements were performed using a confocal microscope equipped with a TCSPC module, with the laser focused at the bottom of the chamber within the contact area of the GUV (Fig. 2A). We select a high-N.A. objective to maximize photon collection efficiency, particularly for emission at angles exceeding the critical angle from dipoles located in close proximity to the MIET substrate (see supporting text 4 and Fig. S1).

Fig. 2B and 2C show the height image of a deflated GUV and a supported lipid bilayer (SLB) on the MIET substrate. The height image was reconstructed from a fluorescence lifetime image acquired by confocal scanning (see Methods for reconstruction details) (*43, 46, 48*). GUV deflation was evidenced by the non-circular geometry of the contact area on the MIET substrate (Fig. 2B). Fig. 2D-a, Fig. 2D-b, and Fig. 2D-c display the measured intensity trace $I(t)$, the calculated height trace $h(t)$, and the brightness trace $br(t)$, respectively, with a time-bin width of 100 µs, where the mean number of photons per time bin was ~ 210. Based on the dynaMIET analysis, we successfully separated iACF into contributions from lateral lipid diffusion and from vertical undulations of the membrane (Fig. 2E). Moreover, we determined the translational diffusion coefficient of membrane lipids as D = 6.75 µm^2/s by fitting the iACF $g_i(t)$ with eq. 6.

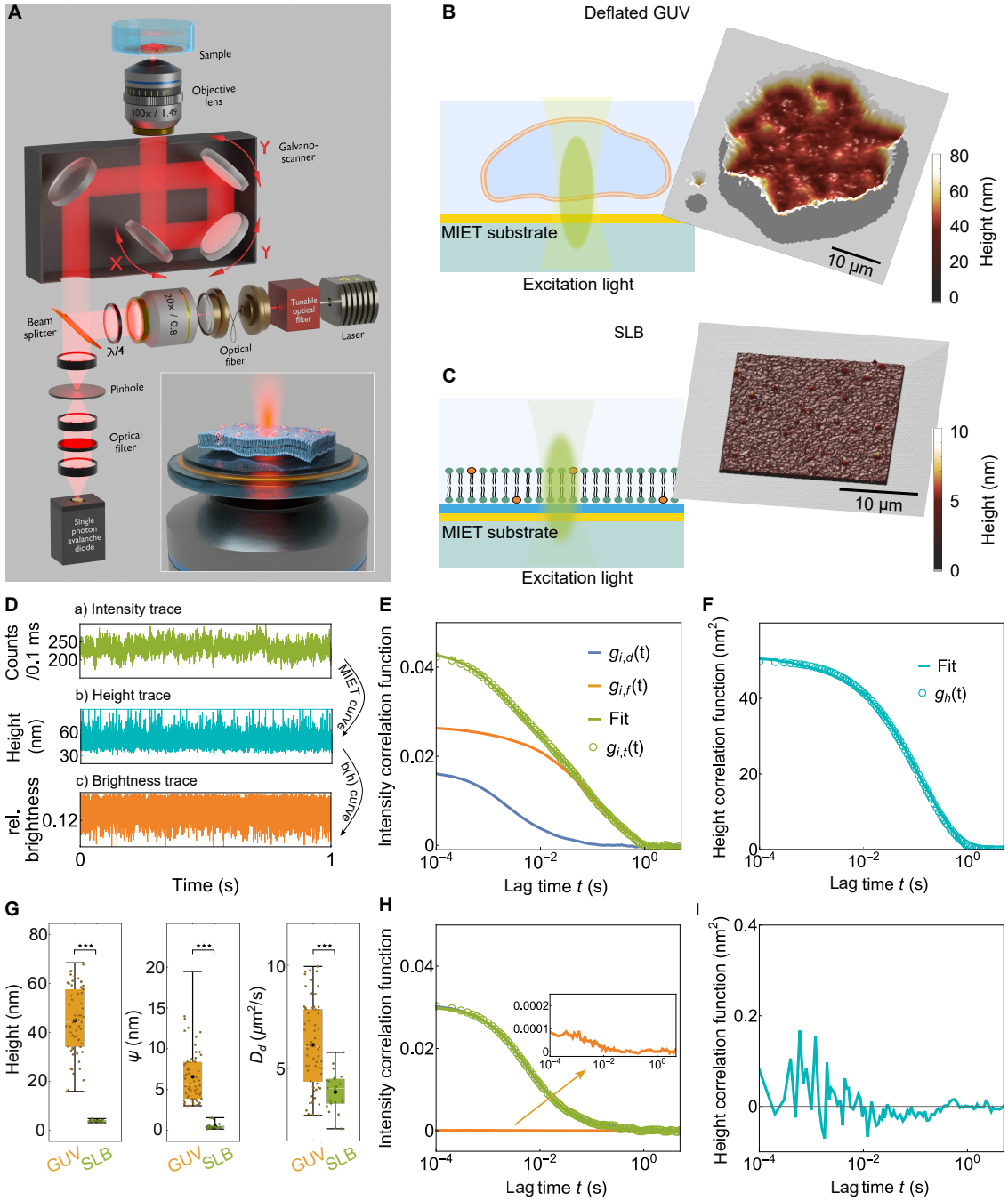

Figure 2: **Validation of dynaMIET on model membrane.**

(A) Illustration of the dynaMIET setup. (B) Schematic of a dynaMIET experiment on a GUV above a MIET substrate. In the upper panel, exemplary 3D reconstructions (height image) of the proximal membrane of a deflated GUV on a MIET substrate are shown, with height encoded by color. (C) Calculated fluorescence intensity time trace (a), height trace (b), and brightness trace (c) for the proximal membrane of one deflated GUV. (D) Various fluorescence iACFs derived from measurements of the proximal membrane of surface-immobilized GUVs on a MIET substrate. The green solid line represents a fit with Eq. 6. (E) Calculated hACF (dotted lines) for the same deflated GUV. Fit values obtained from fitting the hACF with eq 2 (solid line) are also shown. (F) Schematic of a dynaMIET experiment on an SLB deposited on a MIET substrate. In the upper panel, exemplary 3D height profiles of the SLB on the MIET substrate. Height values are encoded by color. (G) Box plots for mean height value h_0, height correlation amplitude ψ, and diffusion coefficient D. Box plots show the 25th–75th quantiles (box), median (white line), mean (black dot), and whiskers (minima to maxima). We performed $n = 22$ independent measurements over 2 independent experiments for SLBs, and $n = 65$ independent measurements over 4 independent experiments for deflated GUVs. Significance levels P were evaluated by a Mann-Whitney U-test: $P < 0.001$ ($\star\star\star$), $P < 0.01$ ($\star\star$), $P < 0.05$ ($\star$). (H) Fluorescence iACFs derived from planar SLB supported on a MIET substrate. The green solid line is fitted with eq 6. Inset shows an enlarged plot of the height-fluctuation-related iACF. (I) Calculated hACF (dotted lines) for the same SLB.

Subsequently, we derived an hACF to assess vertical membrane undulations (Fig. 2F). The membrane height fluctuations of the deflated GUVs exhibit a larger amplitude, characterized by a root mean square height fluctuation of $\psi = 6.6 \pm 3.2$ nm and a relaxation time of $\tau^* = 59 \pm 55$ ms (mean ± SD, $n = 65$). This observation is consistent with our previous measurements using a high-label-concentration method (*44*), and aligns well with values obtained using RICM (h_0 = 31–49 nm and ψ = 4–15 nm) (*51*) and DODS (~ 60 ms) (*29*). Notably, our SOPC results are also very similar to published results on DMPC membranes measured using FLIC microscopy (h_0 = 30–60 nm and ψ = 10 nm) (*55–57*).

The measured hACF ($g_h(t)$) can be effectively modeled using a theoretical framework outlined in Refs. (*51–54*)). The model parameters are the membrane bending rigidity κ, the membrane tension σ, the effective viscosity η, and an interaction potential S that characterizes the coupling between

the fluctuating membrane and the substrate. The hACF is modeled by the following equation:

$$\langle \delta h(t')\delta h(t'+t)\rangle_{t'} = \frac{k_B T}{2\pi}\int_{q_{\min}}^{q_{\max}} dq \frac{q}{\kappa q^4 + \sigma q^2 + S} \exp\left[-S(q)t - \frac{1}{4}w^2 q^2\right] \tag{2}$$

where w denotes the diameter of the confocal detection area. The relaxation rate $S(q)$ includes hydrodynamics and wall effects next to a solid support and is defined by

$$S(q) = \frac{\kappa q^4 + \sigma q^2 + S}{2\eta q} \frac{\sinh^2(qh_0) - (qh_0)^2}{\sinh^2(qh_0) + \sinh(2qh_0)/2 + qh_0(1 - qh_0)} \tag{3}$$

The integration boundaries of the integral in eq. (2) are $q_{\min} = (S/\kappa)^{1/4}$ and $q_{\max} = 1/h_0$ (*54*). When applying this model to describe the hACF of SOPC membranes, we fixed the value of the bending modulus to $\kappa = 20\, k_B T$ as reported in the literature (*29, 58*). We approximated the effective viscosity as the arithmetic mean of the viscosity of buffer solutions inside and outside the GUV, yielding $\eta \sim 1.2$ mPas. The diameter of the confocal detection area in our measurement was determined as $w = 280$ nm by measuring the FCS of a sample with a known diffusion coefficient. We acquired 65 hACF measurements and fitted them with the model; a representative hACF curve (same data point for Fig. 2F) and the corresponding fitted curve are shown in Fig. 2F. From these fits, we derived a surface tension value of $\sigma = 13 \pm 12$ μJm^{-2} (mean ± SD, n = 65) and an interaction potential strength value of $S = 8 \pm 6$ MJm^{-4} (mean ± SD, n = 65), in excellent agreement with published results for similar GUVs (*44, 51–53*).

As a control, we performed dynaMIET measurements on an SLB on a MIET substrate (Fig. 2B). We compared the parameter values obtained from the SLB measurements with those obtained from the deflated GUVs (Fig. 2G). An SLB is a planar membrane on a substrate with only a thin hydration layer of only 1 ∼ 2 nm between the substrate and the membrane (Fig. 2G). Consequently, an SLB can be considered as a membrane without any vertical undulations. As anticipated, the brightness-related iACF is nearly flat, indicating that all intensity fluctuations arise from the lateral diffusion of lipid molecules (Fig. 2H). Similarly, the observed hACF amplitude for an SLB is negligible (ψ = 0.54 ± 0.41 nm, mean ± SD, n = 22, Fig. 2I).

The diffusion coefficients for deflated GUVs obtained with dynaMIET and with conventional FCS (measured on a glass substrate for deflated GUVs, see Fig. S2) are very close to each other (dynaMIET: 6.13 ± 2.03 μm^2/s; conventional FCS: 6.5 ± 2.0 μm^2/s). The diffusion coefficient $D = 3.85 \pm 0.95$ μm^2/s ($n = 22$) of lipid diffusion in an SLB is considerably slower than that of

lipids in a deflated GUV (D = 6.13 ± 2.03 μm^2/s, n = 65). This difference is due to the fact that lipid diffusion in the proximal leaflet of an SLB is impeded by a strong interaction between the lipids and the solid support.

To further validate the capability of dynaMIET to resolve changes in membrane dynamics, we investigated GUV fluctuation dynamics under different temperatures and buffer osmolalities. In model GUV systems, changes in temperature and buffer osmolality are expected to alter membrane tension and available excess area, thereby modifying both the amplitude and timescale of membrane undulations. Consistent with this expectation, dynaMIET measurements reveal statistically significant differences in the structure and 3D dynamics of deflated GUVs across different temperature and osmolality conditions (Fig. S3), supporting its applicability as a quantitative tool for probing membrane mechanics.

The 3D dynamics of the model GUV membrane, as measured with dynaMIET, align well with existing theoretical models and provide reliable values for parameters such as diffusion coefficient, undulation amplitudes, membrane tension, and energy dissipation. These results establish dynaMIET as an accurate and robust technique, which we next apply to investigate the more complex membranes of live cells.

3D dynamics of the cellular plasma membrane

The PM is a very dynamic structure involved in various cellular functions, including cell motility, cell division, or vesicle trafficking. PM undulations span a broad temporal range, with slow actin waves inducing large-wavelength membrane oscillations at cell edges with time durations of seconds. These oscillations involve vertical membrane undulations that range from 100 nm to 10 μm (*59*). In the basal membrane, smaller amplitude undulations are observed, because of the presence of the extracellular matrix (ECM) between the PM and the substrate. Although pronounced membrane undulations are associated with processes such as cell spreading and motility, even subtle, nanometer-scale fluctuations can modulate the spatial organization of molecules within the plasma membrane. These small-amplitude height variations can promote the formation of nanodomains and membrane invaginations, thereby shaping local biochemical organization (*60*).

We applied dynaMIET to resolve the 3D dynamics of the basal membrane COS7 cells cultured

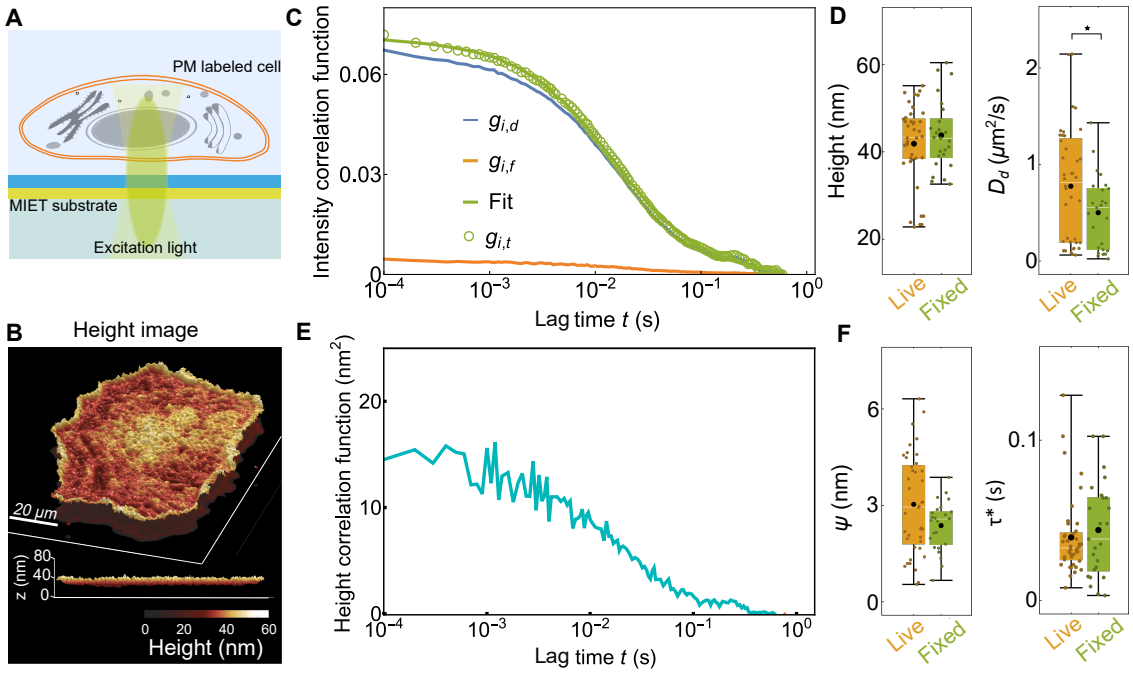

Figure 3: **dynaMIET measurement on a cellular PM.** (A) A schematic of the dynaMIET experiment conducted on a PM-labeled cell on top of a MIET substrate. (B) Reconstructed 3D topography of the fluorescently labeled basal PM of a living COS7 cell on a MIET substrate. The bottom panel offers an alternative viewing angle. Height is color-coded for clarity. (C,E) Same as Fig. 2C, D, but for the PM system. $n = 40$ independent measurements over 3 independent experiments for living cells, and $n = 25$ independent measurements over 2 independent experiments for fixed cells. Data are obtained from independent measurements on multiple cells. For each cell, only 1–2 independent measurements were collected to avoid pseudo-replication. Independent experiments refer to measurements performed on different days using independently prepared samples. (D,F) Box plots of mean height values h_0, diffusion coefficients D, fluctuation amplitudes ψ, and relaxation times $\tau*$ for living and fixed cells.

on a MIET substrate with a 10 nm silica spacer, where the PM was labeled with the commercial PM stain CellMask Deep Red. dynaMIET measurements were performed on the basal membrane of both living and fixed cells (Fig. 3A). Fig. 3B displays reconstructed 3D height maps of the basal membrane of COS7 cells. As can be seen, the distance between the basal membrane and the substrate varies between 35 nm and 55 nm. We randomly chose different points in different cells for the DYNAmiet measurement of the temporal dynamics of PM undulations (Fig. 3C-F).

Fig. 3D shows that the average height values of the membrane appear to be unaffected by the biological activity of a cell, measuring 41.9 ± 9.2 nm (mean ± SD, n = 40) in living cells and 43.8 ± 7.9 nm (mean ± SD, n = 25) in fixed cells (Fig. 3D). Notably, faster lipid diffusion was observed in living cells, with a 1.5-fold increase compared to fixed cells. Specifically, the diffusion coefficients were 0.50 ± 0.38 $\mu m^2/s$ for fixed cells and 0.77 ± 0.59 $\mu m^2/s$ for living cells (Fig. 3D). PM undulations were minimal in both living and fixed cells (Fig. 3F). Living cells exhibited only ~1.3 times larger undulation amplitudes (3.03 ± 1.54 nm) and ~1.4 times slower fluctuation times (28 ± 23 ms) than fixed cells (2.37 ± 0.75 nm and 39 ± 24 ms, respectively) (Fig. 3F). Considering that cross-linked proteins in fixed cells hinder active dynamics, our observations suggest that both active (energy-driven) and passive (thermal fluctuations) processes contribute to basal PM dynamics, in agreement with previous findings using alternative techniques (*60*). The increase in the fluctuation time after cell fixation implies a stiffening of the PM (*61*).

3D dynamics of ER

The ER is a subcellular organelle responsible for numerous essential cellular processes. Within living cells, the ER exhibits high dynamism, continuously undergoing shape remodeling. Although the relationship between ER dynamics and function is not fully understood, recent findings associate abnormal ER dynamics with various diseases (*62*). Previous reports have categorized ER dynamics in mammalian cells into three types: oscillations of established network elements, dynamics of particles within the ER lumen or membrane, and generation of new network elements (*62*). Quantifying ER dynamics remains a formidable challenge due to the complex nature of its movement.

We performed a dynaMIET measurement on ER in COS7 cells on a MIET substrate with a 10 nm silica spacer (Fig. 4). For live-cell imaging, the ER was labeled with the commercial dye

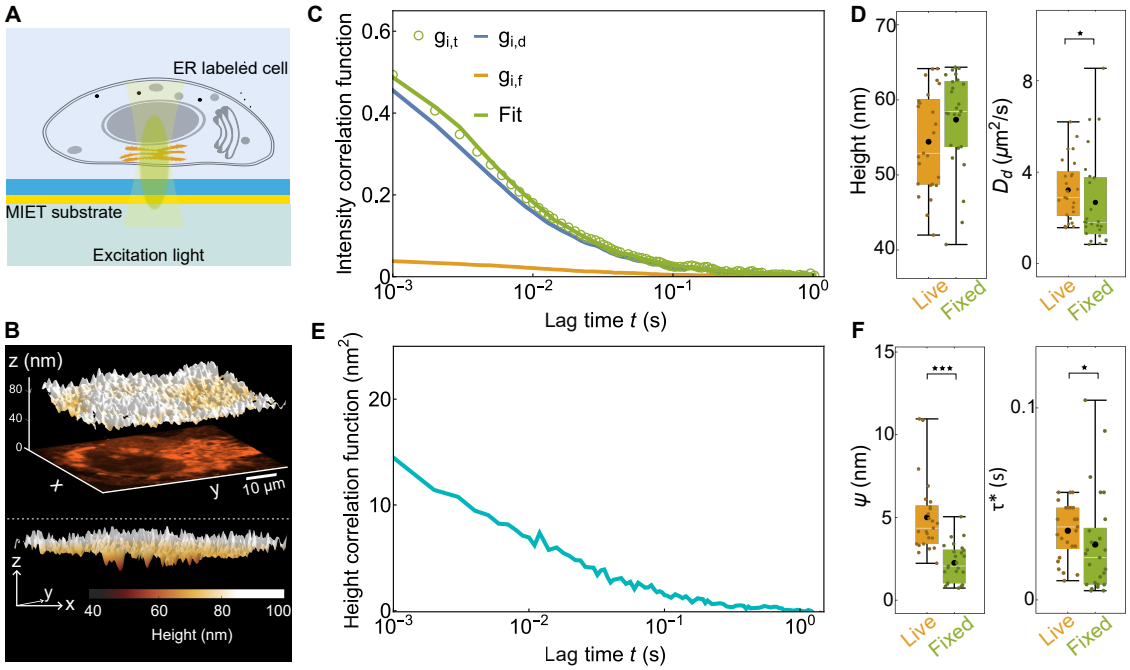

Figure 4: **dynaMIET measurement on ER.** (A, C-F) Same as Fig. 2, but for the ER system. $n = 25$ independent measurements over 3 independent experiments for both living cells and fixed cells. Experimental replication and statistical details are the same as described in Fig. 3. (B) Exemplary 3D reconstructions (height maps) of fluorescently labeled ER in a live COS7 cell on a MIET substrate. The xy-image shows the fluorescence intensity. The bottom panel shows the height image from a different viewing angle.

ER-Tracker Red. In Fig. 4B, we present 3D reconstructed height maps of the labeled ER in a living cell. The distance between the substrate and the ER exhibits considerable variation, ranging from 50 nm to 120 nm. It is important to note that the signal observed from a confocal microscope represents a spatial average over the size of the excitation focus (approximately 300 nm) and over vertical regions of around 500 nm (Fig. 4A). Therefore, the height images in Fig. 4B may not depict a single ER bilayer, rather an average value across the confocal volume. Notably, some locations in Fig. 4B show very low height values (approximately 50 nm), which can be attributed to contact sites between the ER and the PM (*63*). During ER point measurements, a fraction of the detected fluorescence originates from ER regions that are inside the confocal detection volume but outside the MIET-sensitive range (≥ 200 nm from the surface), contributing non–distance-sensitive background to the signal. This can impact the measurement results of ER dynamics within the MIET working range. To minimize the impact of out-of-MIET ER contributions and the presence of multiple ER sheets in the focus of excitation, we excluded data that show an average ER height greater than 65 nm (see Fig. S4 and Supplementary Text).

The results shown in Fig. 4C-F show that we can distinguish between the lateral diffusion of lipids from the perpendicular membrane undulation components in the dynamics of the ER. Comparative dynaMIET experiments were conducted on living and fixed cells. Our findings do not reveal a significant difference between the average membrane heights h_0 in both cases, with measured values of 54.4 ± 6.7 nm for living cells and 57.4 ± 6.5 nm for fixed cells (mean ± SD, n = 25 for living cells and n = 25 for fixed cells, Fig. 4D). However, significant differences are observed for all other parameters. The fluctuation amplitude ψ exhibits a 50% decrease in fixed cells compared to living cells, measuring 5.0 ± 2.2 nm for living cells and 2.3 ± 1.2 nm for fixed cells (Fig. 4F). The diffusion coefficient decreased by approximately 17% after fixation, from 3.2 ± 1.3 $\mu m^2/s$ in live cells and 2.7 ± 2.0 $\mu m^2/s$ in fixed cells. Finally, the correlation relaxation time τ^* showed a 20% decrease from 36 ± 14 ms in living cells to 28 ± 26 ms in fixed cells (Fig. 4F). The substantial reduction in the amplitude of undulation ψ from living cells to fixed cells can be attributed to the fact that the dynamics of ER is predominantly determined by the active motion of the cytoskeleton network and motor proteins (*64, 65*).

3D dynamics of the nuclear envelope

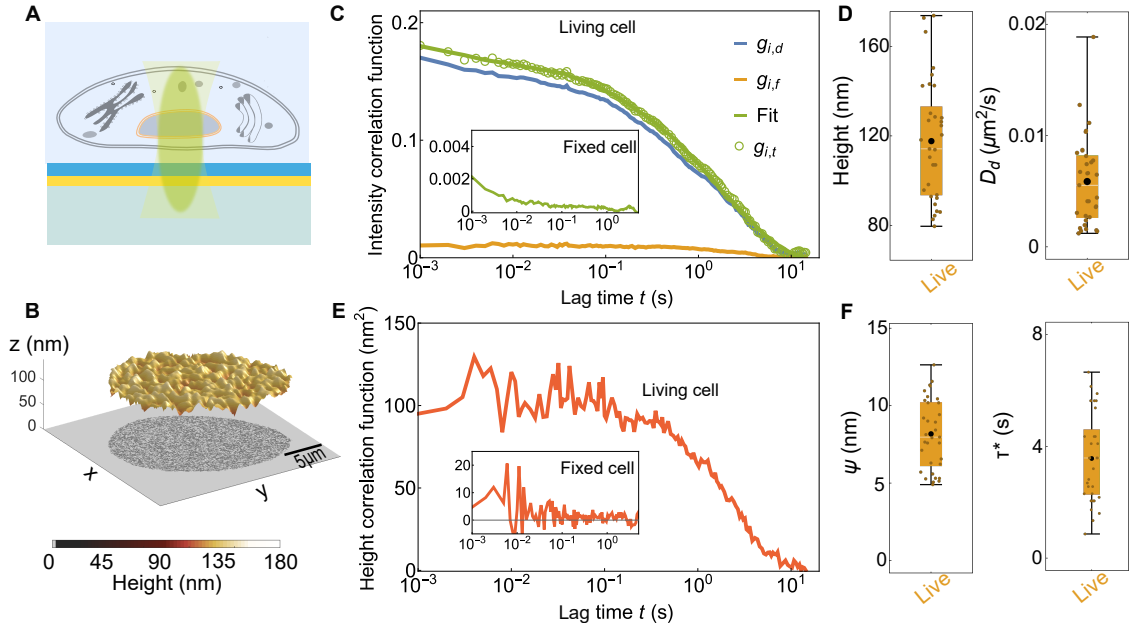

Figure 5: **dynaMIET measurement of NE dynamics.** (A-F) Same as Fig. 3, but for the NE system. n = 33 independent measurements over 3 independent experiments. Experimental replication and statistical details are the same as described in Fig. 3. (C) iACFs obtained from living eGFP-nup153-modified COS7 cell. The green solid line represents a fit with eq 6. The inset shows measured g_i for a fixed cell. (E) Calculated hACF for a living and a fixed cell (inset).

The NE serves as the physical boundary between the cytoplasm and the nucleoplasm, separating two highly dynamic systems: the cellular cytoskeleton and nuclear chromatin. We performed dynaMIET measurements on live and fixed COS7 cells expressing eGFP fused to the nuclear pore protein Nup153, see Fig. 5A and Fig. S5. Fig. 5B shows the measured height profile of the proximal part of the nuclear envelope, showing an average height value of approximately 130 nm, well within the working distance of MIET.

Fig. 5C shows iACFs for NE Nup153 lateral diffusion and membrane undulations in living cells. The observed diffusion is ca. 100 times slower than values measured for lipid diffusion in deflated GUVs, with a diffusion coefficient of only 0.0059 ± 0.0040 µm^2/s (n = 33, Fig. 5D). The relaxation time of NE membrane undulations is also 60 times slower than that for deflated

GUV, determined to be on the timescale of seconds (3.6 ± 1.6 s, Fig. 5F), in good agreement with previous measurements (*66, 67*). The slower dynamics of the NE compared to other cellular membranes can be attributed to its double-bilayer structure, and to strong links to the cytoskeleton on the cytoplasmic side and to the chromatin on the nucleoplasmic side.

Our results show no diffusion or undulations of NE in fixed cells (Fig. 5C,E inset), where the amplitude of the measured total iACF is only 0.002 or 100 times smaller than its value measured in living cells. This is attributed to the heavy cross-linking between the NE and the cytoskeleton and nuclear proteins in the fixed cells. The small residual iACF amplitude may be due to triplet-state photophysics of the eGFP labels. The hACF is too noisy to allow for determining reliable values of relaxation time and amplitude.

Discussion

We introduced dynaMIET as a robust and accessible method for probing the 3D dynamics of biological membranes in both *in vitro* and *in cell* systems. By integrating the nanometer axial precision of MIET with the microsecond temporal resolution of FCS, dynaMIET enables simultaneous quantification of lateral diffusion and vertical membrane undulations. This approach is straightforward to implement on any standard confocal microscope with FLIM modality, and crucially, it requires no empirical calibration, as the necessary calibration curves can be directly and accurately computed from theoretical models.

We demonstrated the versatility of dynaMIET through a wide range of applications, including measurements on GUV membranes, and several cellular membrane systems, such as PM, ER, and NE. From these measurements, we extracted a suite of key biophysical parameters, including diffusion coefficients, fluctuation amplitudes, relaxation times, membrane tension, and membrane–substrate interaction strengths. These insights are particularly valuable for understanding how the mechanical environment, such as substrate adhesion or cytoskeletal coupling, influences membrane organization and function. Beyond model membranes, we demonstrated the usefulness of dynaMIET for membrane studies in living and fixed cells.

dynaMIET offers notable scalability and flexibility, ranging from single point measurement setup to fast-scanning FCS or camera-based wide-field fluorescence lifetime imaging (*68*). This

compatibility will enable spatially resolved mapping of membrane dynamics across large cellular areas while maintaining nanometer axial sensitivity and millisecond temporal resolution. Furthermore, combining dynaMIET with dual-labeling strategies, where both membrane lipids and proteins are independently labeled, opens exciting possibilities for probing protein–membrane interactions at nanometer scales. This includes tracking how peripheral or transmembrane proteins modulate local membrane curvature, tension, or lipid mobility, which are key physical parameters in signaling, vesicle trafficking, and organelle biogenesis.

By providing access to full 3D membrane dynamics, dynaMIET reports on the dynamic coupling between the plasma membrane, membrane proteins, and the underlying cytoskeleton, which is actively regulated during processes such as signaling, adhesion, and membrane trafficking. Changes in these coupled dynamics therefore provide a sensitive readout of alterations in cellular mechanical regulation and membrane protein functions that are not accessible from static membrane height measurements alone. We anticipate that dynaMIET will evolve into a potent and versatile tool for investigating membrane biophysics, particularly in the realms of nanoscale structure and microsecond fluctuations. This methodology holds promise for diverse applications and contexts within the field.

Materials and Methods

Experimental Design

MIET theory

This fluorophore-metal interaction can be modeled in a semi-classical approach based on Maxwell's equations. For this purpose, one considers the fluorescent molecule as an ideal electric dipole emitter and calculates its electromagnetic field in the presence of the MIET substrate, as detailed in Refs. (*69, 70*). This allows for the calculation of the total dipole emission rate (inverse radiative decay rate of the excited fluorophore) as a function of dipole position, orientation (expressed by the angle β between its dipole axis and the vertical direction) and geometry and electrodynamic properties (complex-valued refractive indices) of the substrate. Together with the knowledge of the fluorescence quantum yield ϕ (the ratio of radiative to total transition rate), one then obtains

values of the observable fluorescence lifetime $\tau_f(h,\beta)$ and brightness $b(h,\beta)$ of a fluorophore as a function of its distance h and orientation angle β as

$$\frac{\tau_f(h,\beta)}{\tau_0} = \frac{S_0}{\phi S(h,\beta) + (1-\phi)S_0} \tag{4}$$

$$b(h,\beta) \propto \int_0^{\pi/2} d\beta \sin\beta \frac{N(h,\beta)}{S(h,\beta)} C(h,\beta) \tag{5}$$

In Eq. 4, $S(h,\beta)$ represents the total emission power of the emitter, where S_0 stands for the emission power of an electric dipole emitter with unity quantum yield in a homogeneous unbounded dielectric medium with a refractive index n, where the emitter has fluorescence lifetime τ_0 (free-space fluorescence lifetime). Moving to Eq 5, $N(h,\beta)$ is the total far-field emission radiated into the lower half space (glass coverslip), while $C(h,\beta)$ signifies the relative proportion of emission collected by the objective lens. The angular dependence of $S(h,\beta)$ can be decomposed as $S(h,\beta) = S_\perp(h)\cos^2\beta + S_\parallel(h)\sin^2\beta$, where $S_\perp(h)$ and $S_\parallel(h)$ are the radiative emission rates of emitters oriented perpendicular and parallel to the substrate, respectively. This decomposition extends similarly to $N(h,\beta)$ and $C(h,\beta)$. A detailed mathematical explanation is given in supporting text 4. It is crucial to note that the functions $S_\perp(h)$ and $S_\parallel(h)$ are solely dependent on h.

Simulation of membrane diffusion and fluctuation near a gold surface.

To investigate the fluorescence signal modulated by membrane dynamics near a plasmonic interface, we performed numerical simulations of fluorescent particle diffusion on a fluctuating lipid membrane positioned above a gold surface. The lateral diffusion of particles was modeled as two-dimensional Brownian motion within a $50\,\mu\text{m} \times 50\,\mu\text{m}$ box with periodic boundary conditions, using a diffusion coefficient $D = 5.0\,\mu\text{m}^2/\text{s}$, particle surface concentration $C = 40\,\text{particles}/\mu\text{m}^2$, and a Gaussian excitation beam with a waist of $\omega = 0.3\,\mu\text{m}$. Membrane height fluctuations were simulated using an Ornstein-Uhlenbeck method with a mean height $z_0 = 40\,\text{nm}$, standard deviation $\sigma_z = 10\,\text{nm}$, and correlation time $\tau_c = 50\,\text{ms}$, reflecting thermal motion within a constrained potential. Each simulation included 10^5 time steps with a temporal resolution of $\Delta t = 0.1\,\text{ms}$, for a total simulated duration of 10 seconds per run. The process was repeated 10 times to obtain averaged statistical results. Fluorescence intensity at each time point was computed by summing the Gaussian-weighted contributions of all particles within the focal area, modulated by the instantaneous membrane height using precomputed MIET brightness and lifetime calibration curves. The

MIET parameters were: free-space fluorescence lifetime $\tau_{\text{free}} = 1\,\text{ns}$, fluorophore quantum yield $QY = 0.8$, emission wavelength $\lambda = 700\,\text{nm}$, and a multilayer structure composed of 2 nm Ti / 10 nm Au / 1 nm Ti / 10 nm SiO_2. Autocorrelation functions were calculated from the resulting time traces to disentangle the contributions of diffusion and vertical membrane fluctuations to the observed FCS signal. To further assess the robustness of the method, we additionally performed simulations with a higher fluorophore occupancy ($C = 150\,\text{particles}/\mu\text{m}^2$, average 43 molecules within the confocal volume, see Fig. S6). The resulting simulated dynamics are consistent with those obtained at lower concentration, demonstrating that the analysis is robust with respect to fluorophore number.

dynaMIET analysis flow chart

Measured fluorescence intensity fluctuations can be analyzed by calculating an intensity autocorrelation function $g_{i,t}(t)$ (iACF). The value of the iACF for a lag time t is defined as the time average of the product of intensity deviations from the mean value at time, t' $\delta I(t') = I(t') - \langle I \rangle$, and at time $t' + t$, $\delta I(t' + t) = I(t' + t) - \langle I \rangle$, i.e. $g_i(t) = \langle \delta I(t') \delta I(t' + t) \rangle$, where the angular brackets denote averaging over time t'. As mentioned in main text, in the presence of a MIET substrate, the total iACF $g_{i,t}(t)$ can be divided into a part $g_{i,d}(t)$ related to the lateral diffusion of single lipids, a part $g_{i,f}(t)$ related to vertical undulations of the membrane, and a part $g_{i,tri}(t)$ related to the triple state relaxation of the fluorophore (see eq. 4).

We separated the $g_{i,d}(t)$ and $g_{i,f}(t)$ by so-called TTTR single-photon counting. For each detected photon, TTTR provides two timestamps: the macrotime that counts the number of laser pulses between the start of the measurement and the photon detection, and the microtime that is the delay time between the last laser pulse and the photon detection. The macrotime is utilized for computing intensity traces and the iACF $g_{i,t}$, while the microtime is used to calculate the fluorescence lifetime.

In our dynaMIET analysis (Fig. S7), we start with computing an intensity trace $I(t)$ over time bins with width Δ t = 100 µs or 1ms, which is then used to calculate the iACF $g_{i,t}(t)$ (Fig. S7i, after photobleaching correction, see Fig. S8 and Supplementary Text). Subsequently, we determine the fluorescence lifetime within each time bin by computing the square root of the variance of the microtimes recorded during each time bin (Fig. S7ii). An ideal fast lifetime estimation should have

less than 10 % uncertainty, which requires approximately 100 photons (*71, 72*). This determines the minimum width of the time binning: one needs approximately 100 photons per time bin for a reasonable lifetime estimate. Taking into account that the maximum photon detection rate that a single photon detector can handle is typically around 4,000 kcps (kilo counts per second), one obtains a minimal possible time bin width of 25 µs. However, the photon detection rate varies as a function of fluorophore brightness and concentration, which results in a varying temporal resolution for different samples (see Supplementary Text and Fig. S9). It should be noted that, to satisfy the photon count requirements for reliable fluorescence lifetime estimation, a relatively higher labeling concentration than that used in conventional FCS is required. In the present experiments, approximately 30–60 molecules were present within the confocal volume, and extended acquisition times were employed to improve correlation statistics.

In the next step, each fluorescence lifetime per time bin is converted into a height value using the lifetime-versus-height calibration curve (Fig. 1C, blue curve), resulting in a continuous trace of height values $h(t)$ (Fig. 1D-c). Furthermore, relying on the brightness-height calibration curve (Fig. 1C, yellow curve), a relative brightness trace ($br(t)$) is obtained (Fig. 1D-d), facilitating the direct computation of the MIET-induced height-related correlation function ($g_{i,f}(t) = \langle br(t')br(t'+t)\rangle_{t'} / \langle br(t)\rangle^2$). For $g_{i,d}(t)$, the diffusion can be described with a 2D diffusion model, $g_{i,d} = 1/(N(1+t/t_D))$, where N is the total molecules in the confocal volume and τ_D is the diffusion time of lipids through the confocal volume Therefore, from Eq. 1, combining all the contributions, the iACF $g_{i,t}(t)$ can be fitted with following model:

$$g_{i,t}(t) = \left[1 + \frac{F\exp(-t/\tau_T)}{1-F}\right] \frac{g_{i,f}(t)}{N(1+t/\tau_D)} \tag{6}$$

where F and τ_T are the triplet state amplitude and time that take into account the triplet state pumping and decay of the used fluorophores. Finally, the diffusion coefficient D is determined from $D = w^2/(4\tau_D)$, where w is the beam waist of the laser excitation focus in the plane of the membrane.

The height trace $h(t)$ provides information about the vertical undulations of a membrane. It can be decomposed into a mean value h_0 plus a deviation from this mean value $\delta h(t)$, i.e. $h(t) = h_0 + \delta h(t)$. The temporal dynamics of these membrane undulations can be characterized by the height autocorrelation function $g_h(t) = \langle \delta h(t')\delta h(t'+t)\rangle_{t'}$ (hACF).

dynaMIET measurement

dynaMIET measurements were conducted using a custom-built confocal microscopy setup. The excitation sources comprised a pulsed diode laser (λ_{exc} = 640nm, LDH-D-C 640, PicoQuant) for red dye and a white laser (NKT Photonics, Koheras SuperK Power) with Acousto-Optic Tunable Filters (AOTFnC-400.650-TN, Pegasus Optik Gmbh). The beam was collimated from an infinity-corrected 4x objective (UPISApo 4X, Olympus), then reflected by a dichroic mirror (Di01-R405/488/561/635, Semrock) towards a high numerical aperture objective (UApoN 100X, oil, 1.49 N.A., Olympus). Emission light was focused into a pinhole with a diameter of 100 µm and refocused onto one avalanche photodiode (τ-SPAD, PicoQuant). A long-pass filter (BLP01-647R-25, or LF561/LP-D-000, or LF488/LP-C-000, Semrock) and a band-pass filter (Brightline HC692/40, or FF01-609/54-25, or FF01-525/45-25, Semrock) were positioned before the pinhole and the detector, respectively. Single-count data from the detector were processed using a multi-channel picosecond event timer (Hydraharp 400, PicoQuant). Imaging scanning was facilitated by a fast Galvo scanner (FLIMbee, Picoquant). The microscope is equipped with a diagnostic back-reflection camera at the conjugate image plane. Back reflected laser at the MIET substrate interface provides a reliable way to position and monitor the excitation focus at the interface. In addition to this, the focus position stability within ±5 nm is ensured during long point FCS data acquisition with an active home-built autofocus drift correction system. The system is based on monitoring the back-reflected signal of an auxiliary infrared (IR) laser (850 nm, 3.5 mW; Thorlabs, CPS850S) incident on the substrate interface. The IR beam is focused onto an off-center region of the objective back focal plane. The back-reflected IR light from the substrate interface is imaged onto a camera (Mako U130B, Allied Vision) placed at a conjugate image plane. Axial displacement of the sample relative to the focal plane leads to a measurable change in the position of the back-reflection pattern on the camera. This signal is continuously monitored and used as an error signal for focus stabilization. A feedback loop actively corrects axial drift by adjusting the sample position via the piezo-controlled z-stage, thereby maintaining the excitation focus at the membrane. The performance of the autofocus system is illustrated by a representative time trace of the z-position (Fig. S10), demonstrating that axial position fluctuations are constrained within ±5 nm over extended acquisition times.

For live cell measurements, a microscopy-based incubator (ibidi Stage Top Incubation System-

Blue Line, ibidi) maintained controlled conditions (temperature: 37°C, CO_2 concentration: 5%, humidity: 40%). In a typical measurement, the sample was initially scanned at the MIET substrate surface to determine the contour of the GUVs or cells. Subsequently, an appropriate point position was selected for single-point acquisition, and data were recorded for at least 2 minutes for each data point. All measurements were completed within 1.5 h after cell staining to ensure consistent experimental conditions. The sample within the working distance of MIET can be determined by its fluorescence curve (Fig. S11).

The height image was reconstructed from the fluorescence lifetime image following previously published MIET protocols (*43,46,48*). Briefly, to accurately determine membrane height, individual cells were scanned to accumulate sufficient photon counts for reliable fluorescence decay fitting. TCSPC decay curves were constructed for each pixel and fitted using a multiexponential decay model, yielding the mean fluorescence lifetime at each pixel. These lifetime images were then converted into membrane height maps relative to the substrate using the MIET calibration curve.

Substrate preparation

We followed the procedures outlined in our previous publications (*43, 70*) to prepare the gold-modified substrate. A layer-by-layer deposition technique was used, where 2 nm of titanium, 10 nm of gold (or 40 nm for SLB measurement), 1 nm of titanium, and 10 nm of SiO_2 were successively electron-beam evaporated onto the surface of a glass coverslip. The electron-beam evaporation was carried out using a Univex 350 electron beam source (Leybold) under high-vacuum conditions (approximately 10^{-6} mbar). To ensure maximal homogeneity, the deposition was conducted at the slowest rate (1 $\mathring{A}s^{-1}$). The spacer thickness was continuously monitored during the evaporation process using an oscillating quartz unit. This gold-covered substrate is referred to as the MIET substrate.

Prior to the MIET experiment, the MIET substrate underwent plasma cleaning for 60 seconds at the highest plasma intensity (Harrick Plasma). For cell experiments, the MIET substrates were sterilized under UV illumination for 30 min prior to use. For GUV experiments, the MIET substrate was incubated in a 5 mg/mL^{-1} solution of BSA (Sigma-Aldrich, A3294) for 15 minutes to prevent nonspecific interactions, followed by ten washes with PBS buffer.

Vesicles and SLB preparation

SLB was prepared through the fusion of small unilamellar vesicles (SUVs), which were generated using an extrusion method. A 100 µL mixture containing 10 mg/mL 1,2-Dioleoyl-sn-glycero-3-phosphocholine (DOPC, Avanti Polar Lipids, 850375C) lipids and 0.05 mol% DPPE-atto655 (ATTO-TEC, AD-655-151) lipids in chloroform (Sigma-Aldrich, 132950) was dried in a vacuum for 1 h at 30 °C. The resulting lipid film was then re-dispersed in 500 µL of PBS buffer (pH = 7.4) and shaken for 1 h at 37°C. SUVs were obtained by extruding the solution through a polycarbonate filter (Whatman) with a 50 nm pore diameter for 15 cycles. The SLB was prepared by incubating the SUV solution on the MIET substrate for 1 h at room temperature, followed by washing with PBS buffer.

GUVs made of SOPC (Avanti Polar Lipids, 850467C) were fabricated using the electro-formation method (*70*). A 100 µL lipid mixture containing 10 mg/mL SOPC, 2 mol% 1,2-dioleoyl-sn-glycero-3-phosphoethanolamine-N-(methoxy(polyethylene glycol)-2000) (PEG2000-PE, Avanti Polar Lipids, 880130C), and 0.05 mol% DPPE-atto655 was deposited on two steel electrodes and evaporated for 3 h under vacuum at 30 °C. The electrodes were sealed with a Teflon chamber and filled with 500 µL of sucrose solution (230 mM). The chamber was subjected to an alternating electric current at 15 Hz for 3 h with a peak-to-peak voltage of 1.6, followed by 8 Hz for 30 min. After electro-formation, the GUVs suspension was stored at −4°C and used within 3 days. The GUVs suspension was diluted 50 times in PBS buffer (400 $mOsml^{-1}$ or 450 $mOsml^{-1}$, 10mM Na_2HPO_4, 2mM KH_2PO_4, 3 mM KCl, and ~ 180 mM (or ~ 205 mM for 450 $mOsml^{-1}$) NaCl, pH 7.4) for the observation of floppy GUVs. The osmolality of the PBS buffers was measured using an osmometer (Gonotec® Osmomat 3000 Basic) and adjusted to desired values by adding 1 M NaCl. For all GUV experiments, the diluted GUVs solution with observation buffer was added to a chamber (Culture-Insert 4 Well, ibidi GmbH) on the MIET substrate. A glass slide covered the chamber, and the setup was left undisturbed for 10 min at room temperature for equilibration before the measurement.

Cell culture and membrane labeling

COS7 monkey kidney cell (ATCC, CRL-1651) was a gift from Prof. Silvio Rizzoli (University Medicine Göttingen). The cells were cultured at 37°C in 5% CO2 in T-75 culture flasks using Dulbecco's Modified Eagle's Medium (DMEM) - high glucose (Sigma, D6429-500L) supplemented with 10% fetal bovine serum (Sigma-Aldrich, F7524) and 1% penicillin/streptomycin (Sigma, P4333). Cells were seeded onto 35-mm glass-bottom dishes (Ibidi, 81158), either gold-coated or uncoated, at 8×10^4 cells per dish and cultured for 24 h. For experiments using fixed cells, samples were washed with PBS and fixed in 4% paraformaldehyde/PBS solution for 20 minutes.

ER-Tracker Red (0.5 µM solution in DMEM, ER-Tracker™ Red, ThermoFisher, E34250) and CellMask Deep Red (500 ng/mL solution in DMEM, CellMask™ Plasma Membrane Stains, ThermoFisher, C10046) were used for specific labeling of the ER and PM, respectively. The labeling protocols strictly followed the manufacturer's instructions. Cells were incubated with the labeling solution for 20 min at 37 °C, followed by replacement of the staining solution with fresh, probe-free DMEM medium. For NE labeling, cells were transfected one day before imaging with the pEGFP(C3)-Nup153 plasmid encoding fluorescent nucleoporin-153 (*73*) using Effectene Transfection Reagent (Qiagen, 301425). pEGFP(C3)-Nup153 was a gift from Birthe Fahrenkrog (Addgene plasmid # 64268; http://n2t.net/addgene:64268; RRID:Addgene_64268).

Statistical Analysis

All values are expressed as the mean ± SD. All box plots show the 25th–75th quantiles (box), median (white line), mean (black dot), and whiskers (minima to maxima). Significance levels P were evaluated by a Mann-Whitney U-test: $P < 0.001$ (★★★), $P < 0.01$ (★★), $P < 0.05$ (★). No statistical method was used to predetermine sample size. All experiments were conducted in at least two independent replicates, yielding reproducible results. In each experiment, measurements were performed on multiple cells or GUVs, and only 1–2 independent measurements were collected per cell or GUV to avoid pseudo-replication. For the ER measurements, data with ER heights exceeding 65 nm were excluded, with a detailed explanation provided in the Supplementary Text 3.

References and Notes

1. K. Simons, E. Ikonen, Functional rafts in cell membranes. *Nature* **387** (6633), 569–572 (1997), doi:10.1038/42408.

2. B. Alberts, *et al.*, *Molecular Biology of the Cell* (Garland Science, New York, NY), 6th ed. (2015).

3. H. Noguchi, Nonequilibrium membrane dynamics induced by active protein interactions and chemical reactions: A review. *ChemSystemsChem* **7** (1), e202400042 (2025).

4. M. Baaden, Visualizing biological membrane organization and dynamics. *Journal of molecular biology* **431** (10), 1889–1919 (2019).

5. D. Lingwood, K. Simons, Lipid rafts as a membrane-organizing principle. *Science* **327** (5961), 46–50 (2010), doi:10.1126/science.1174621.

6. H. T. McMahon, J. L. Gallop, Membrane curvature and mechanisms of dynamic cell membrane remodelling. *Nature* **438** (7068), 590–596 (2005), doi:10.1038/nature04396.

7. A. Sciortino, *et al.*, Active membrane deformations of a minimal synthetic cell. *Nature Physics* pp. 1–9 (2025).

8. R. Phillips, J. Kondev, J. Theriot, H. G. Garcia, *Physical Biology of the Cell* (Garland Science, New York, NY), 2nd ed. (2012).

9. N. H. Linh, *et al.*, Molecular dynamics simulation of cancer cell membrane perforated by shockwave induced bubble collapse. *The Journal of Chemical Physics* **157** (22) (2022).

10. J. Lee, K. Sengupta, Exploring membrane organization at varying spatiotemporal resolutions utilizing fluorescence-based approaches: implications in membrane biology. *Physical Chemistry Chemical Physics* **21** (23), 12075–12090 (2019), doi:10.1039/C9CP02087J.

11. L. de Armas-Rillo, M.-S. Valera, S. Marrero-Hernández, A. Valenzuela-Fernández, Membrane dynamics associated with viral infection. *Reviews in medical virology* **26** (3), 146–160 (2016).

12. D. J. Selkoe, Alzheimer's disease: genes, proteins, and therapy. *Physiological Reviews* **81** (2), 741–766 (2001), doi:10.1152/physrev.2001.81.2.741.

13. L. Julian, M. F. Olson, Apoptotic membrane dynamics in health and disease. *Cell Health and Cytoskeleton* pp. 133–142 (2015).

14. M. D. Rosenblum, K. A. Remedios, A. K. Abbas, Mechanisms of human autoimmunity. *The Journal of Clinical Investigation* **125** (6), 2228–2233 (2015), doi:10.1172/JCI78088.

15. M. P. Sheetz, Cell control by membrane–cytoskeleton adhesion. *Nature Reviews Molecular Cell Biology* **2** (5), 392–396 (2001), doi:10.1038/35073095.

16. A. Pandey, *et al.*, Membrane fluctuation model for understanding the effect of receptor nanoclustering on the activation of natural killer cells through biomechanical feedback. *Nano letters* **24** (18), 5395–5402 (2024).

17. A. Fuhrmann, A. J. Engler, Mechanical regulation of cell function with implications for tumor progression and metastasis. *Seminars in Cell & Developmental Biology* **47-48**, 2–13 (2015), doi:10.1016/j.semcdb.2015.07.002.

18. M. L. Dustin, J. T. Groves, Receptor signaling clusters in the immune synapse. *Annual Review of Biophysics* **41**, 543–556 (2012), doi:10.1146/annurev-biophys-042910-155238.

19. J. Rossy, Y. Ma, K. Gaus, The organization of the cell membrane: do proteins rule lipids? *Current Opinion in Chemical Biology* **17** (6), 746–750 (2013), doi:10.1016/j.cbpa.2013.06.016.

20. S. Takamori, *et al.*, Molecular anatomy of a trafficking organelle. *Cell* **127** (4), 831–846 (2006), doi:10.1016/j.cell.2006.10.030.

21. C. B. Jackson, M. Farzan, B. Chen, H. Choe, Mechanisms of SARS-CoV-2 entry into cells. *Nature Reviews Molecular Cell Biology* **23** (1), 3–20 (2022), doi:10.1038/s41580-021-00418-x.

22. S. Klein, A. Pekosz, Virus entry by endocytosis. *Advances in Virus Research* **98**, 1–40 (2017), doi:10.1016/bs.aivir.2016.07.002.

23. J. B. Klauda, M. F. Roberts, A. G. Redfield, B. R. Brooks, R. W. Pastor, Rotation of lipids in membranes: molecular dynamics simulation, 31P spin-lattice relaxation, and rigid-body dynamics. *Biophysical journal* **94** (8), 3074–3083 (2008).

24. M. Javanainen, O. S. Ollila, H. Martinez-Seara, Rotational diffusion of membrane proteins in crowded membranes. *The Journal of Physical Chemistry B* **124** (15), 2994–3001 (2020).

25. M. S. Miettinen, R. Lipowsky, Bilayer membranes with frequent flip-flops have tensionless leaflets. *Nano letters* **19** (8), 5011–5016 (2019).

26. S. Sanyal, A. K. Menon, Flipping lipids: why an'what's the reason for? *ACS chemical biology* **4** (11), 895–909 (2009).

27. S. Ramadurai, *et al.*, Lateral diffusion of membrane proteins. *Journal of the American Chemical Society* **131** (35), 12650–12656 (2009).

28. P. F. Almeida, W. L. Vaz, Lateral diffusion in membranes. *Handbook of biological physics* **1** (C), 305–357 (1995).

29. C. Monzel, *et al.*, Measuring fast stochastic displacements of bio-membranes with dynamic optical displacement spectroscopy. *Nature Communications* **6** (1), 1–8 (2015).

30. H. Turlier, T. Betz, Unveiling the active nature of living-membrane fluctuations and mechanics. *Annual Review of Condensed Matter Physics* **10**, 213–232 (2019).

31. M. A. McNiven, A. J. Ridley, Focus on membrane dynamics. *Trends in Cell Biology* **16** (10), 485–486 (2006).

32. G. Tomaiuolo, Biomechanical properties of red blood cells in health and disease towards microfluidics. *Biomicrofluidics* **8** (5) (2014).

33. I. Dulińska, *et al.*, Stiffness of normal and pathological erythrocytes studied by means of atomic force microscopy. *Journal of biochemical and biophysical methods* **66** (1-3), 1–11 (2006).

34. N. W. Goehring, D. Chowdhury, A. A. Hyman, S. W. Grill, FRAP analysis of membrane-associated proteins: lateral diffusion and membrane-cytoplasmic exchange. *Biophysical Journal* **99** (8), 2443–2452 (2010).

35. R. Macháň, M. Hof, Lipid diffusion in planar membranes investigated by fluorescence correlation spectroscopy. *Biochimica et Biophysica Acta (BBA)-Biomembranes* **1798** (7), 1377–1391 (2010).

36. A. V. Weigel, B. Simon, M. M. Tamkun, D. Krapf, Ergodic and nonergodic processes coexist in the plasma membrane as observed by single-molecule tracking. *Proceedings of the National Academy of Sciences* **108** (16), 6438–6443 (2011).

37. F. Brochard, J. Lennon, Frequency spectrum of the flicker phenomenon in erythrocytes. *Journal de Physique* **36** (11), 1035–1047 (1975).

38. Y. Park, *et al.*, Metabolic remodeling of the human red blood cell membrane. *Proceedings of the National Academy of Sciences* **107** (4), 1289–1294 (2010).

39. V. R. Singh, *et al.*, Studying nucleic envelope and plasma membrane mechanics of eukaryotic cells using confocal reflectance interferometric microscopy. *Nature communications* **10** (1), 3652 (2019).

40. K. Sengupta, L. Limozin, Adhesion of soft membranes controlled by tension and interfacial polymers. *Physical Review Letters* **104** (8), 088101 (2010).

41. A.-S. Smith, K. Sengupta, S. Goennenwein, U. Seifert, E. Sackmann, Force-induced growth of adhesion domains is controlled by receptor mobility. *Proceedings of the National Academy of Sciences* **105** (19), 6906–6911 (2008).

42. S. F. Fenz, *et al.*, Membrane fluctuations mediate lateral interaction between cadherin bonds. *Nature Physics* **13** (9), 906–913 (2017).

43. A. I. Chizhik, J. Rother, I. Gregor, A. Janshoff, J. Enderlein, Metal-induced energy transfer for live cell nanoscopy. *Nature Photonics* **8** (2), 124–127 (2014).

44. T. Chen, N. Karedla, J. Enderlein, Measuring sub-nanometer fluctuations at microsecond temporal resolution with metal-and graphene-induced energy transfer spectroscopy. *Nature communications* **15**, 1789 (2024).

45. T. Chen, N. Karedla, J. Enderlein, Observation of E-cadherin adherens junction dynamics with metal-induced energy transfer imaging and spectroscopy. *Communications Biology* **7** (1), 1596 (2024).

46. D.-X. Wang, *et al.*, Metal-induced energy transfer (miet) imaging of cell surface engineering with multivalent dna nanobrushes. *ACS nano* **18** (7), 5409–5417 (2024).

47. N. Karedla, D. Ruhlandt, A. M. Chizhik, J. Enderlein, A. I. Chizhik, Metal-Induced Energy Transfer. *Advanced Photon Counting: Applications, Methods, Instrumentation* pp. 265–281 (2015).

48. A. Ghosh, A. I. Chizhik, N. Karedla, J. Enderlein, Graphene-and metal-induced energy transfer for single-molecule imaging and live-cell nanoscopy with (sub)-nanometer axial resolution. *Nature Protocols* **16** (7), 3695–3715 (2021).

49. I. Gregor, A. Chizhik, N. Karedla, J. Enderlein, Metal-induced energy transfer. *Nanophotonics* **8** (10), 1689–1699 (2019).

50. N. Karedla, *et al.*, Three-dimensional single-molecule localization with nanometer accuracy using Metal-Induced Energy Transfer (MIET) imaging. *The Journal of Chemical Physics* **148** (20), 204201 (2018).

51. J. O. Rädler, T. J. Feder, H. H. Strey, E. Sackmann, Fluctuation analysis of tension-controlled undulation forces between giant vesicles and solid substrates. *Physical Review E* **51** (5), 4526 (1995).

52. D. Schmidt, *et al.*, Signature of a nonharmonic potential as revealed from a consistent shape and fluctuation analysis of an adherent membrane. *Physical Review X* **4** (2), 021023 (2014).

53. C. Monzel, *et al.*, Nanometric thermal fluctuations of weakly confined biomembranes measured with microsecond time-resolution. *Soft Matter* **12** (21), 4755–4768 (2016).

54. N. Gov, A. Zilman, S. Safran, Hydrodynamics of confined membranes. *Physical Review E* **70** (1), 011104 (2004).

55. C. Monzel, K. Sengupta, Measuring shape fluctuations in biological membranes. *Journal of Physics D: Applied Physics* **49** (24), 243002 (2016).

56. Y. Kaizuka, J. T. Groves, Structure and dynamics of supported intermembrane junctions. *Biophysical Journal* **86** (2), 905–912 (2004).

57. Y. Kaizuka, J. T. Groves, Hydrodynamic damping of membrane thermal fluctuations near surfaces imaged by fluorescence interference microscopy. *Physical Review Letters* **96** (11), 118101 (2006).

58. C. Monzel, S. F. Fenz, M. Giesen, R. Merkel, K. Sengupta, Mapping fluctuations in biomembranes adhered to micropatterns. *Soft Matter* **8** (22), 6128–6138 (2012).

59. G. Giannone, *et al.*, Periodic lamellipodial contractions correlate with rearward actin waves. *Cell* **116** (3), 431–443 (2004).

60. A. Biswas, A. Alex, B. Sinha, Mapping cell membrane fluctuations reveals their active regulation and transient heterogeneities. *Biophysical Journal* **113** (8), 1768–1781 (2017).

61. J. Seifert, J. Rheinlaender, P. Novak, Y. E. Korchev, T. E. Schäffer, Comparison of atomic force microscopy and scanning ion conductance microscopy for live cell imaging. *Langmuir* **31** (24), 6807–6813 (2015).

62. H. T. Perkins, V. Allan, Intertwined and finely balanced: endoplasmic reticulum morphology, dynamics, function, and diseases. *Cells* **10** (9), 2341 (2021).

63. R. Fernández-Busnadiego, Y. Saheki, P. De Camilli, Three-dimensional architecture of extended synaptotagmin-mediated endoplasmic reticulum–plasma membrane contact sites. *Proceedings of the National Academy of Sciences* **112** (16), E2004–E2013 (2015).

64. Y. Hama, H. Morishita, N. Mizushima, Regulation of ER-derived membrane dynamics by the DedA domain-containing proteins VMP1 and TMEM41B. *EMBO reports* **23** (2), e53894 (2022).

65. M. S. Tikhomirova, A. Kadosh, A. J. Saukko-Paavola, T. Shemesh, R. W. Klemm, A role for endoplasmic reticulum dynamics in the cellular distribution of microtubules. *Proceedings of the National Academy of Sciences* **119** (15), e2104309119 (2022).

66. V. Introini, G. R. Kidiyoor, G. Porcella, P. Cicuta, M. Cosentino Lagomarsino, Centripetal nuclear shape fluctuations associate with chromatin condensation in early prophase. *Communications Biology* **6** (1), 715 (2023).

67. F.-Y. Chu, S. C. Haley, A. Zidovska, On the origin of shape fluctuations of the cell nucleus. *Proceedings of the National Academy of Sciences* **114** (39), 10338–10343 (2017).

68. N. Oleksiievets, *et al.*, Wide-field fluorescence lifetime imaging of single molecules. *The Journal of Physical Chemistry A* **124** (17), 3494–3500 (2020).

69. N. Karedla, *et al.*, Single-Molecule Metal-Induced Energy Transfer (smMIET): Resolving Nanometer Distances at the Single-Molecule Level. *ChemPhysChem* **15** (4), 705–711 (2014).

70. A. Ghosh, *et al.*, Graphene-based metal-induced energy transfer for sub-nanometre optical localization. *Nature Photonics* **13** (12), 860–865 (2019).

71. X. Liu, *et al.*, Fast fluorescence lifetime imaging techniques: A review on challenge and development. *Journal of Innovative Optical Health Sciences* **12** (05), 1930003 (2019).

72. M. Nasser, A. Meller, Lifetime-based analysis of binary fluorophores mixtures in the low photon count limit. *Iscience* **25** (1) (2022).

73. V. Duheron, G. Chatel, U. Sauder, V. Oliveri, B. Fahrenkrog, Structural characterization of altered nucleoporin Nup153 expression in human cells by thin-section electron microscopy. *Nucleus* **5** (6), 601–612 (2014).

74. E. Wolf, Electromagnetic diffraction in optical systems-I. An integral representation of the image field. *Proceedings of the Royal Society of London. Series A. Mathematical and Physical Sciences* **253** (1274), 349–357 (1959).

75. B. Richards, E. Wolf, Electromagnetic diffraction in optical systems, II. Structure of the image field in an aplanatic system. *Proceedings of the Royal Society of London. Series A. Mathematical and Physical Sciences* **253** (1274), 358–379 (1959).

76. V. I. Martynov, A. A. Pakhomov, BODIPY derivatives as fluorescent reporters of molecular activities in living cells. *Russian Chemical Reviews* **90** (10), 1213 (2021).

Acknowledgments

We thank Anna Chizhik for providing the MIET substrates, Ingo Gregor for insightful discussions, Silvio Rizzoli for supplying the cell samples, and Alexey Chizhik for designing and preparing the schematic illustration of the microscope setup.

Funding: This work was supported by:
Deutsche Forschungsgemeinschaft (DFG, German Research Foundation) project consortium SPP 2493/1, projects EN 297/28-1 and JA 963/22-1.
European Research Council (ERC) project “smMIET” no. 884488
Deutsche Forschungsgemeinschaft (DFG, German Research Foundation) Germany’s Excellence Strategy EXC 2067/1-390729940
European Union’s Horizon 2021 research and innovation program, Marie Sklodowska-Curie Grant Agreement no. 101062508 (project name: SOADOPP)
European Research Council (ERC) project “MIETEN” no. 101164162.

Author contributions:
Conceptualization: TC, JE, NK
Data curation: TC, NK
Investigation: TC, JIG, DXW, BZ, LZC
Methodology: TC, JE, NK
Funding acquisition: JE, JIG, NK
Software: TC, NK

Supervision: TC, JE

Visualization: TC, JE

Validation: BZ, LZC

Writing – original draft: TC, JIG, NK

Writing – review & editing: TC, JIG, NK, JE

Competing interests: There are no competing interests to declare.

Data and materials availability: All data supporting the findings of this study are present in the paper and the Supplementary Materials. There are no restrictions on data and code availability. Raw data of this study are publicly available in the Dryad repository at `https://doi.org/10.5061/dryad.xsj3tx9rf`. This repository also contains detailed documentation of the data analysis procedures and processing workflows, including all MATLAB and Python code used in this work. In addition, the code and software are also available online. Specifically, the MIET calculation and analysis code is available on GitHub at `https://github.com/Nkaredla/MIET_calc` and the dynaMIET simulation and analysis code is available on GitLab at `https://gitlab.gwdg.de/tchen1/3dmembranedynamics`. The 3D height profiles were calculated using a freely available MATLAB-based MIET-GUI software (*48*).

Supplementary materials

Supplementary Text

Figs. S1 to S11